Environmental Technology & Innovation 34 (2024) 103604

Contents lists available at ScienceDirect

Environmental Technology & Innovation

journal homepage: www.elsevier.com/locate/eti

Heavy metal and soluble organic matter removal using natural conglomerate and siltstone soils: Towards soil aquifer treatment for oily wastewater

Jisha Kuttiani Ali [a,b], Hala Ghaleb [c], Abdul Fahim Arangadi [a,b], Tu Phuong Pham Le [a,b], Sasi Stephen [d], Mohamed Soufiane Jouini [e], Daniel Moraetis [f], Kosmas Pavlopoulos [c], Emad Alhseinat [a,b,*]

[a] Chemical Engineering Department, Khalifa University of Science and Technology, Abu Dhabi, United Arab Emirates
[b] Center for Membranes and Advanced Water Technology, Khalifa University of Science and Technology, Abu Dhabi, United Arab Emirates
[c] Geography and Planning Department, Sorbonne University, Abu Dhabi, United Arab Emirates
[d] Chemistry Department, Khalifa University of Science and Technology, Abu Dhabi, United Arab Emirates
[e] Mathematics Department, Khalifa University of Science and Technology, Abu Dhabi, United Arab Emirates
[f] Applied Physics and Astronomy Department, University of Sharjah, Sharjah, United Arab Emirates

ARTICLE INFO

Keywords:
Produced water
Adsorption
Aquifer
Heavy metals
Dissolved organics

ABSTRACT

The present work aims to assess the viability of vadose zone siltstone and conglomerate for oil and gas-produced water (PW) treatment using soil aquifer treatment (SAT). Comprehensive batch adsorption tests were carried out to analyze siltstone and conglomerate removal capacity for dissolved organics (phenol), and heavy metal ions (Ni^{2+}, and Zn^{2+}). The results demonstrated that conglomerate displayed a 98% removal capacity for Zn^{2+} and 88% for Ni^{2+} while siltstone showed 82% removal for Zn^{2+} and 88% removal for Ni^{2+}. However, both siltstone and conglomerate showed low phenol removal (32% for siltstone, and 9% for conglomerate). The equilibrium adsorption isotherms were fitted by several adsorption models. The Langmuir model exhibited the best fitting for the adsorptions of phenol, Ni^{2+} ions, and Zn^{2+} ions on the two soils. The kinetics studies have revealed that phenol, Ni^{2+} ions, and Zn^{2+} ions adsorption on the two soil samples obey a pseudo-second-order kinetic model. Furthermore, Fourier transform infrared spectroscopy studies revealed that the Si-O peak in the soil plays a predominant role in interactions with heavy metal ions and phenol due to its high content in the soils. However, the electrostatic interactions between functional groups (Si-O, CO_3^{2-}, and C═O carbonyl groups) of the soil samples and the Ni^{2+} ions, Zn^{2+} ions, and phenol also contributed to the removal capacity. It is revealed that Zn^{2+} has a greater affinity for carboxyl groups than Ni^{2+}. The obtained data in this study would support the effective design of SAT treatment for PW and help in reducing the risk of contaminating the groundwater aquifer.

1. Introduction

Wastewater from the oil and gas sector known as produced water (PW) contains significant levels of hazardous compounds that are

* Corresponding author at: Chemical Engineering Department, Khalifa University of Science and Technology, Abu Dhabi, United Arab Emirates.
E-mail address: emad.alhseinat@ku.ac.ae (E. Alhseinat).

https://doi.org/10.1016/j.eti.2024.103604
Received 26 November 2023; Received in revised form 10 March 2024; Accepted 19 March 2024
Available online 20 March 2024

carcinogenic, teratogenic, and mutagenic. However, if properly treated, this waste-produced water may be utilized for a variety of uses, including irrigation and subterranean water recharge (Jisha Kuttiani Ali et al., 2023; Tibbetts et al., 1992; Kingsley Tamunokuro Amakiri et al., 2022). The majority of oil and gas-producing countries are arid and experience severe freshwater shortages. As a result, there is noticeable interest in developing ecological, cost-effective, and long-term treatment solutions for oil and gas-PW (Gaber, 2023). Current traditional approaches for the treatment of PW, which include physical, chemical, and biological methods, have major drawbacks such as low removal effectiveness of dissolved organics and heavy metals, high costs, high effluent turbidity, and the formation of hazardous sludge (Kingsley Tamunokuro Amakiri et al., 2022; Gaber, 2023). The optimal treatment strategy for PW is determined primarily by water chemistry, available space, cost-effectiveness, reusability, discharge plans, by-products, and long-term operation (Kingsley Tamunokuro Amakiri et al., 2022). Soil aquifer treatment (SAT) is emerging as an attractive method for the treatment of PW due to its high efficiency and low cost compared to other methods (Sharma and Soil, 2017; Grinshpan et al., 2022). Applying SAT technology to PW introduces PW as an unconventional water source for recharging shallow groundwater aquifers (Jisha Kuttiani Ali et al., 2023). SAT enhances the physical, chemical, and microbiological quality of wastewater while allowing long-term storage with no evaporative loss and minimal external re-contamination (Sharma and Soil, 2017). SAT is seen as an appealing component of modern water management technology since it allows for water reuse, conserving freshwater resources, and minimizing wastewater disposal issues (Jisha Kuttiani Ali et al., 2023; Sharma and Soil, 2017).

SAT effectively removes suspended particles, aromatic carbon as well as non-aromatic compounds, trace metals, heavy metals, and pathogens from wastewater (Sharma and Soil, 2017). Hermes et al. (2019) have found that 70 trace organic chemicals found in their feed water were decreased by 60% following 3 days of subsurface treatment using the SAT approach (Hermes et al., 2019). Recently, the applicability of sand and sandstone for SAT was studied. Both soils showed high removal rates for heavy metals and dissolved organics (Jisha Kuttiani Ali et al., 2023). However, considerable uncertainties in the SAT system emerge due to the risk of contaminants leaching into the water aquifers, and problems in optimizing operating parameters. In addition, the chemistry of infiltrating wastewater varies owing to a variety of activities such as organic matter biodegradation, adsorption, ion exchange between pollutants and soil, etc (Sharma and Soil, 2017). Before implementing the SAT technique for PW treatment, it is necessary to conduct a comprehensive evaluation of the effectiveness of removing contaminants by the soil layers in the vadose zone. Additionally, a thorough understanding of the interaction between various soil types and contaminants in PW must be established.

To understand the mechanism that drives the adsorption, Two-dimensional correlation spectroscopy (2D-COS), particularly FTIR spectroscopy has been frequently used (Yang et al., 2019; Noda, 2007). The 2D-COS not only eliminates peak overlaps, which is a major shortcoming of one-dimensional (1D) FTIR but also provides the correlation signals of peaks in FTIR spectra under an external disturbance (Yang et al., 2019; Noda, 2007; Chen et al., 2015; Ji et al., 2009). Hence, FTIR combined with 2D-COS may be a valuable tool for investigating the interactions between functional groups in the soil of the vadose zone with different contaminants in the PW (Jisha Kuttiani Ali et al., 2023). For a deeper understanding of the mechanism of adsorption, it is useful to use 2D-COS FTIR to examine the interactions of contaminants with functional groups of adsorbate and thereby their extents in the removal process (Jisha Kuttiani Ali et al., 2023; Yang et al., 2019).

There has been little or no research into the efficacy of conglomerate and siltstone for the PW treatment using the SAT technique. The current study looked at the applicability of siltstone and conglomerate from the vadose zone, Abu Dhabi, United Arab Emirates for the SAT technique of PW treatment. The removal capacity of conglomerate and siltstone on phenol and heavy metals (Ni^{2+} and Zn^{2+}) is assessed here by artificially created PW. Batch tests were done on a laboratory scale without changing the pH at room temperature for 336 hours. The results were compared to different isotherms and kinetics models. The 2D correlation analysis combined with FTIR in attenuated total reflectance geometry was used to evaluate the different kinds of interaction between soil samples and contaminants (Ni^{2+}, Zn^{2+}, and phenol).

2. Materials and methods

2.1. Reagents

The heavy metal salts such as Ni $(NO_3)_2.6\ H_2O$ (97%), Zn $(NO_3)_2.6\ H_2O$ (99%), and phenol (99.5%) were sourced from Sigma-Aldrich. The experiments were done using deionized water (18 MΩ cm) and all chemicals were used without further purification.

2.2. Soil sample collection

The conglomerate and siltstone were collected by shallow core sampling method from Abu Dhabi, UAE. The depth of the sample's location for conglomerate and siltstone was maintained at 10.8 m. The collected soil samples were directly transferred to the laboratory in airtight bags. The homogenized samples using a grinder were transferred to plastic containers and kept at room temperature. Before starting the experiments, conglomerate, and siltstone were kept in the oven for 48 h at 90 ℃.

2.3. Batch experiments

For batch studies, 1000 mg/L concentration of stock solutions in 500 mL quantity of heavy metals (Zn^{2+} ion, Ni^{2+} ion), and phenol were prepared separately in deionized water (DI). The initial experimental concentrations of Ni^{2+}, Zn^{2+}, and phenol were fixed at 5 mg/L for Ni^{2+}, and Zn^{2+}, and 20 mg/L for phenol; these concentrations are the same as in produced water (Tibbetts et al., 1992; Kingsley Tamunokuro Amakiri et al., 2022). Then batch tests were conducted using conglomerate and siltstone to investigate their

removal performance against Ni^{2+}, Zn^{2+}, and phenol without adjusting their pH and maintaining them at room temperature. The experimental factors such as the soil/solution ratio, time on maximum adsorption, and effects of concentration of contaminants were studied. The two replicates for all experiments were done using fresh soil samples. The UV-Vis spectrophotometer (DR 6000, Hach) along with suitable LCK kits was used for monitoring the changes in concentration of the Ni^{2+} ion, Zn^{2+} ion, and phenol. The LCK kits such as LCK 360, LCK 337, and LCK 345 for Ni^{2+} ion, Zn^{2+} ion, and phenol were used, separately.

The removal efficiency ®, and adsorption capacity at equilibrium (q_e) of soil samples against Ni^{2+}, Zn^{2+}, and phenol were determined using Eqs. (1) and (2), respectively (Jisha Kuttiani Ali et al., 2023)

$$\text{Removal efficiency}(\%) = \frac{(C_i - C_e)}{C_i} \times 100 \tag{1}$$

$$qe = \frac{(C_i - C_e)}{W} \times V \tag{2}$$

where C_i and C_e denote initial concentrations (mg/L), and equilibrium concentrations (mg/L) of the adsorbate: W (g) and V (L) represent the mass of the adsorbent, and solution volume, respectively

3. Results and discussion

3.1. Characterization of conglomerate and siltstone

The mineral composition and morphology of the conglomerate and siltstone were analyzed by employing different characterization techniques. According to the result of FTIR spectra of soils, as shown in Figure S1, conglomerate, and siltstone displayed a strong band at 1000 cm^{-1}, which represents Si-O asymmetric stretching, which confirmed the existence of silica-based minerals in both soil samples (Xiao et al., 2022; Shahata, 2016). The FTIR peaks that appeared at 2000 cm^{-1}, and 1415 cm^{-1} indicated the in-plane bending band and the asymmetric stretching band of CO_3^{2-}, respectively, in the conglomerate spectrum representing the presence of carbonate-based minerals in conglomerates such as dolomite and calcite (Ji et al., 2009; Hao et al., 2018; Cai et al., 2010). The less intense band at 2000 cm^{-1} in siltstone confirms the presence of carbonate-based minerals which is lesser in concentration compared to that in conglomerate (Ji et al., 2009). In addition, the bands at 1612 cm^{-1}, and 2100 cm^{-1} indicate the existence of C═O groups of carboxylate, and carbonyl compounds in siltstone.

To confirm the mineralogical composition of conglomerate and siltstone, the XRD analysis

was conducted. Fig. 1 shows that the conglomerate and siltstone have sharp crystalline peaks and observed peaks in the range of 5–100 at 2 theta value revealed that both samples were a mixture of minerals such as quartz, calcite, dolomite, smectite, and illite (Ji et al., 2009; Al-Jaroudi et al., 2007; Bruckman and Wriessnig, 2013; Kaczmarek et al., 2017). To identify the different elements present in both soil samples, XRF analysis was done and results showed that 35.5% of SiO_2 was present in conglomerate and 43% of SiO_2 was found in siltstone along with the low percentages of P_2O_5, K_2O, Fe_2O_3, SO_3, TiO_2, and MgO (Table 1). As seen in Table 1, the conglomerate consists of the maximum amount of CaO (19.7%) and a lower amount of FeO (0.8%), while siltstone has higher FeO (2.8%) and only 3.3% of CaO. The sum of all compounds is not close to 100% due to the absence of Na_2O, and Al_2O_3 in the analysis. These results support the XRD analysis and FTIR analysis and reveal that the conglomerate is distinctive from siltstone in mineral percentage and thus geochemistry is also different compared with siltstone.

The morphology of conglomerate and siltstone was analyzed using SEM at different magnifications. Fig. 2 (a1 and a2) displays that the conglomerate has rod-shaped morphology formed by agglomeration of rhombohedral calcite seeds (blue arrows in Fig. 2 (a1, and

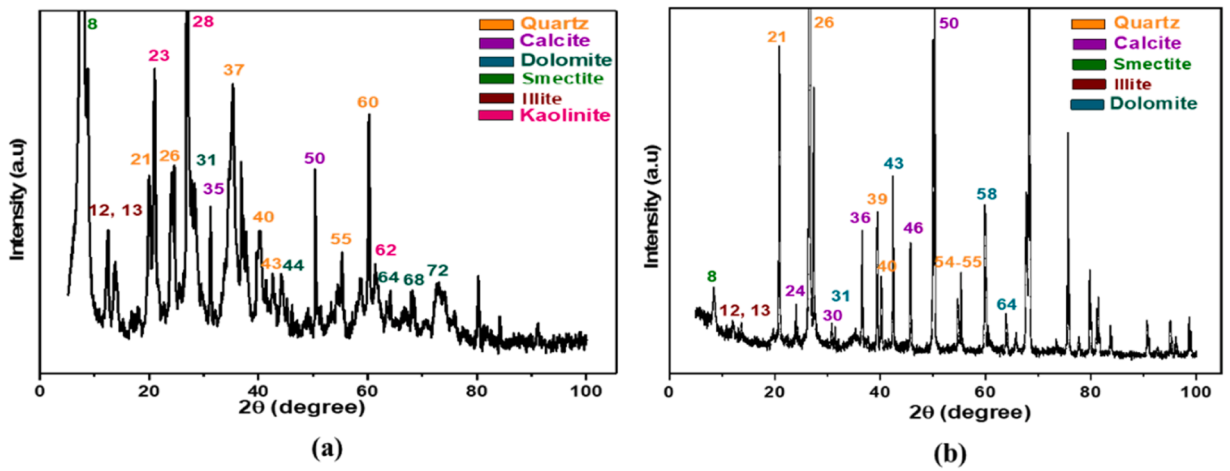

Fig. 1. XRD spectra of (a) Conglomerate, and (b) Siltstone.

Table 1
Elemental composition from XRF analysis.

	SiO_2	CaO	P_2O_5	K_2O	Fe_2O_3	SO_3	MgO	Al_2O_3	Na_2O	TiO_2	LOI	SUM
Conglomerate	35.5	19.7	0.3	1.0	0.8	< DL	15.7	Not measured	Not measured	0.5	22.5	96
Siltstone	43.0	3.3	0.5	0.9	2.8	0.2	5.1	Not measured	Not measured	0.2	18.4	74.4

DL: below detection limit

a2) whereas, silica spheres were spread on the rhombohedral sheets (red arrows in Fig. 2(a2)) which is the indication of quartz minerals (Ali, 2014; Shahwan et al., 2005; Kim et al., 2014). While siltstone appeared with less in rhombohedral calcite seeds (blue arrows in Fig. 2(b1 and b2)). The spherical silica particles were distributed on the sheets along with rhombohedral morphology (red arrows in Fig. 2(b2) (Vos et al., 2014; Guven et al., 2015). These images revealed the presence of calcite and silica in both soil samples in which calcite has a higher concentration in conglomerate compared to siltstone composition.

To evaluate the chemical composition, EDX line spectra and EDX mapping of conglomerate and siltstone were collected. The results are summarized in Figures S2 and S3. As shown in Figures S2 and S3, both soils were rich in silicon, with less calcium along with other elements such as magnesium, aluminum, and iron, which is consistent with XRF analysis.

3.2. Effects of the amount of soil

The effects of the amount of conglomerate/siltstone on the removal performance of contaminants were monitored and results were summarized in Fig. 3(a). As shown in Fig. 3(a), the removal performance of siltstone was gradually enhanced when the dosage of soil samples increased for Ni^{2+}, Zn^{2+}, and phenol. The siltstone presented the highest removal of 96.4% for Ni^{2+}, 95.8% for Zn^{2+}, and 28.2% for phenol at the dosage of 500 mg/L. For the conglomerate, the removal percentage for Zn^{2+} was 96–99%, and for Ni^{2+} was 89–94.5% for an adsorbent ratio of 250 mg/L, and 500 mg/L, respectively (Fig. 3(b)). However, the removal performance for phenol was enhanced with conglomerate dosages and was a maximum of 15.2% at a ratio of 500 mg/L. The high removal efficiency is attributed to the more available sites for adsorption at higher dosages of adsorbent (Mishra et al., 2017).

3.3. Effect of contact time on adsorption

To estimate the equilibrium time for maximum removal, siltstone and conglomerate were put for 336 hours in solutions of Ni^{2+}, Zn^{2+}, and phenol. As shown in Fig. 4, the removal percentages of conglomerate and siltstone for Ni^{2+}, Zn^{2+}, and phenol exhibited accelerated values within the first 24 h. Insignificant changes were noted after 24 h. Moreover, the removal of Ni^{2+} and Zn^{2+} with siltstone and conglomerate showed 48 h to reach maximum adsorption. These results are matched with the studies by Noppadol

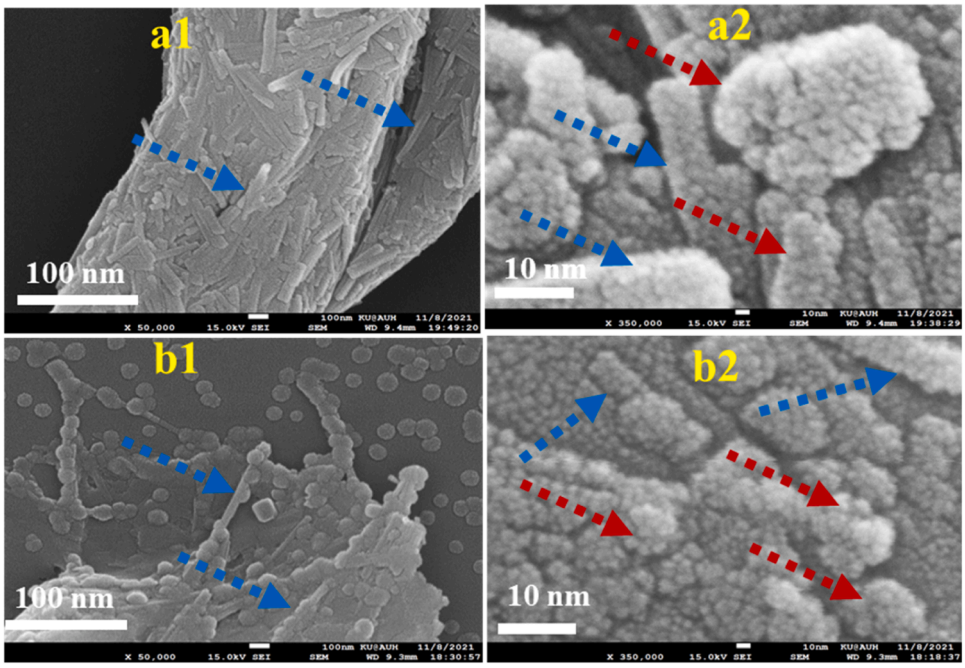

Fig. 2. SEM images of (a) Conglomerate and (b) Siltstone (1, and 2 represent the 50,000X, and 350, 000X magnification and red arrows denote the spherical silica, and blue arrows indicate the rhombohedral calcite).

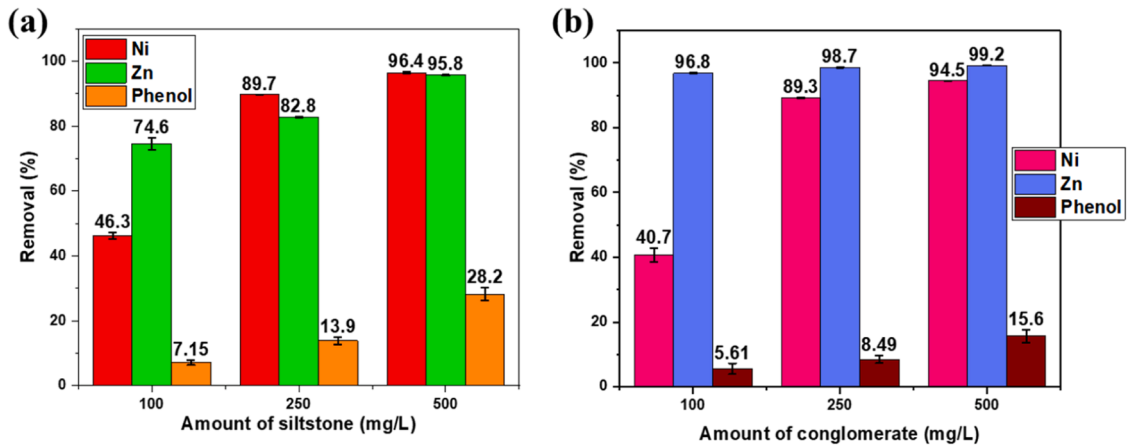

Fig. 3. Effect of amount of soil samples (a) siltstone and (b) conglomerate on sample solution of Ni^{2+}, Zn^{2+}, and phenol; Experiment conditions: concentration of Ni^{2+}, and Zn^{2+} are 5 mg/L, and 20 mg/L for phenol; 336 h is the contact time and experiment was conducted at room temperature without changing the pH; error bars (±1 standard deviation (SD) of the mean of two replicates of experiments).

Sangiumsak et al. (2014) (Noppadol Sangiumsak, 2014). As shown in Fig. 4, the removal percentage of siltstone for Ni $^{2+}$, Zn^{2+}, and phenol were 88%, 82%, and 32%, respectively, and for the conglomerate, the removal rate was 88% 98%, and 9% for Ni $^{2+}$, Zn^{2+}, and phenol, respectively. The excellent removal efficiency of both soil samples for heavy metal ions may be related to the effectiveness of different minerals present in both samples, for the removal of Ni^{2+} and Zn^{2+}, rather than phenol.

3.4. Kinetics study results

The pseudo-first-order kinetic model (PFO), pseudo-second-order kinetic model (PSO), and Elovich's kinetic model (EK) were applied for evaluating the adsorption kinetics of Ni^{2+}, $Zn^{2+}$and phenol on siltstone and conglomerate (Jisha Kuttiani Ali et al., 2023; Salari et al., 2022). The experiment was conducted with 5 mg/L for Ni^{2+} and Zn^{2+}, 20 mg/L for phenol, and 0.250 mg/g of adsorbent by varying agitation time (1–336 h). The contaminant's concentration was measured in different time intervals by UV-Vis spectrophotometer.

The Eq. (3) represents PFO and the amount of heavy contaminants adsorbed at equilibrium (q_e (mg/g)), and PFO rate constant (K_1 (h^{-1})) calculated from the linear plot of $\ln(q_e\text{-}q_t)$ versus t, respectively (Jisha Kuttiani Ali et al., 2023; Mishra et al., 2017; Liu et al., 2021).

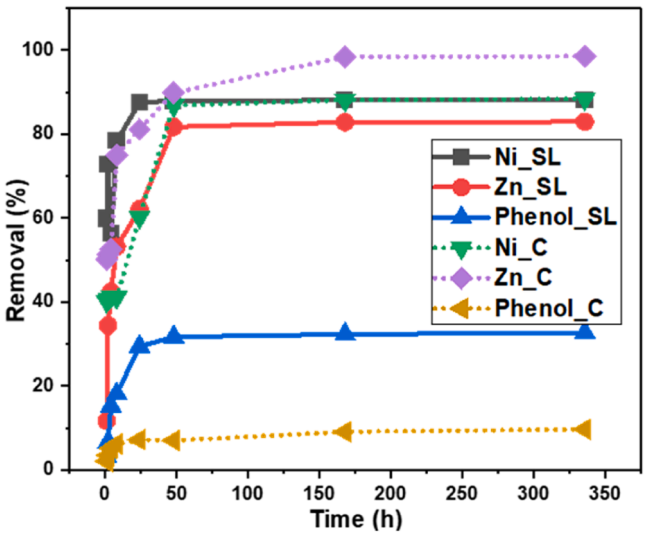

Fig. 4. Effect of contact time on the removal performance of contaminants; Experiment conditions: the amount of siltstone and conglomerate is 250 mg/L; concentration of Ni^{2+} and Zn^{2+} are 5 mg/L and 20 mg/L for phenol; 336 h is the contact time and experiment was conducted without changing the pH at room temperature; Dotted lines for the conglomerate and solid lines for siltstone; C represents the conglomerate and SL represents the siltstone.

$$\ln(q_e - q_t) = \ln q_e - K_1 \tag{3}$$

where q_t indicates the amount of adsorbed contaminants at time t (h).

Eq. (4) represents PSO and the plot of t/qt versus t provides the amount of heavy contaminants adsorbed at time t (q_e (mg/g)), and PSO rate constant (K_2 (h^{-1})):

$$\frac{t}{q_t} = \frac{1}{K_2 {q_e}^2} + \frac{1}{q_e} \tag{4}$$

The Eqs. (5) and (6) indicate Elovich's kinetic model (EK) and its linear form. The plot of ln(t) versus q_t provides the initial adsorption rate (A ((mg/g h)) and the extent of surface coverage and activation energy for chemisorption (B (g/mg)), respectively (Jisha Kuttiani Ali et al., 2023; Caceres-Jensen et al., 2021).

$$\frac{dq_t}{dt} = ae^{(-bq_t)} \tag{5}$$

$$q_t = \ln\left(\frac{AB}{B}\right) + \frac{1}{B}\ln(t) \tag{6}$$

Figures S4-S6 summarized the three kinetics models such as PFO, PSO, and EK models for the adsorption of Ni^{2+}, $Zn^{2+,}$ and phenol on siltstone and conglomerate. The kinetics parameters were obtained from the plot of respective kinetic models summarized in Table S1. As shown in Table S1, for PFO, and Elovich's kinetic model, lower R^2 values indicated that the adsorption of phenol, $Ni^{2+,}$ and Zn^{2+} ions did not follow PFO, and Elovich's kinetic model. Moreover, the calculated q_e value for both samples with heavy metal ions and phenol did not match the experimental q_{exp} value for PFO, and Elovich's kinetic model. However, the PSO showed the highest R^2 denoting this as the most suitable model. The calculated q_e values from the PSO model for both adsorbents perfectly correlated with experimental q_{exp}, for all contaminants. The results of these kinetics studies are consistent with the literature (Mishra et al., 2017; Shikuku et al., 2018).

3.5. Effects of concentration of contaminants

The effects of the initial concentrations of phenol, $Ni^{2+,}$ and Zn^{2+} ions on the siltstone and conglomerate were investigated in a series of concentrations from 5 mg/L to 20 mg/L. Here, the soil dosage was 250 mg/L, and experiments were conducted at room temperature without changing the pH. As seen in Fig. 5, the removal performance decreased when the concentration of contaminants changed to 20 mg/L from 5 mg/L for both soil samples. For Ni^{2+} and Zn^{2+}, siltstone shows a 50%, and 65% reduction in removal performance when the concentration of Ni^{2+} and Zn2+ reached 20 mg/L. A similar effect was also noted for the removal performance of conglomerates with heavy metal ions at higher concentrations. Furthermore, at higher phenol concentrations (20 mg/L), a 50% reduction in removal performance was noted for siltstone, while insignificant change in removal performance was observed with conglomerate. These results suggested that the initial concentration of Ni^{2+}, $Zn^{2+}$and phenol significantly distressed the removal efficiency of siltstone and conglomerate. This is attributed that at a fixed dosage of adsorbents if the concentration of contaminants increases the removal performance gradually reduces as the ratio of adsorption sites to adsorbates decreases (Mishra et al., 2017).

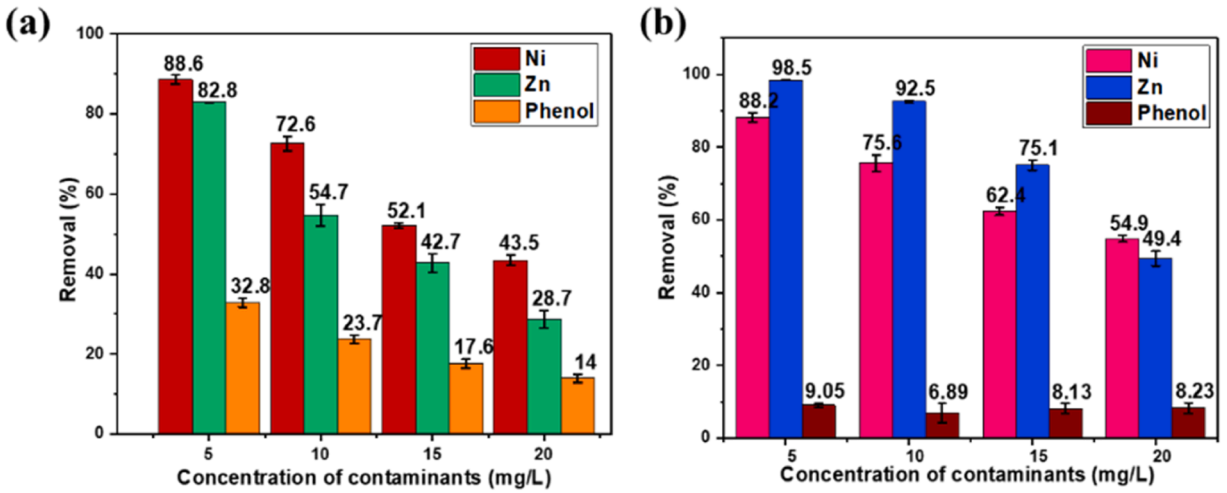

Fig. 5. Effect of concentration of contaminants (a) siltstone, and (b) conglomerate; Experiment conditions: the amount of siltstone, and conglomerate is 250 mg/L; contact time is 336 h and the experiment was conducted at room temperature without changing the pH; error bars (±1 standard deviation (SD) of the mean of two replicates of experiments).

3.6. Adsorption isotherms

To monitor the affinity of Ni^{2+}, Zn^{2+}, and phenol towards soil samples, the concentration of contaminants at equilibrium versus adsorption capacity at equilibrium was plotted and displayed in Figure S7. As seen in Figure S7, both soil samples presented the Langmuir-type (L-shaped) isotherm for Ni^{2+}, Zn^{2+}, and phenol except conglomerate for phenol. The L-type isotherm indicated that soil samples have a high affinity for Ni^{2+}, Zn^{2+}, and phenol ions at low concentrations, but as the concentration increase, the affinity of contaminants decreased because the active sites in adsorbents are preoccupied (Flores et al., 2009; Sipos et al., 2005). Whereas isotherm of phenol with conglomerate exhibited a C–-type curve suggesting a partitioning mechanism for phenol with conglomerate (Shikuku et al., 2018; Sipos et al., 2005; Sparks, 2002). That is, phenol was distributed or partitioned between the bulk solution phase and interfacial phase without forming any specific interaction with the conglomerate. In this case, phenol showed less removal than 9% for conglomerate as displayed in Fig. 3.

The adsorption capacity of siltstone and conglomerate could be determined by analyzing the adsorption of Ni^{2+}, Zn^{2+}, and phenol at equilibrium. An adsorption isotherm reveals information about the maximum adsorption capacity, and characteristics of the surface (Salari et al., 2022).

In the Langmuir adsorption isotherm model, it is monolayer adsorption of adsorbate onto the surface of an adsorbent (Jisha Kuttiani Ali et al., 2023). Eqs. (7) and (8) represent Langmuir's isotherm and linear Langmuir's isotherm, respectively. The linear Langmuir isotherm obtained from the plot of $1/C_e$ versus $1/qe$ gives information about the adsorption-desorption equilibrium constant (K_L), maximum adsorption capacity (q_{max}), and regression constant (R^2) values (Mishra et al., 2017).

$$qe = \frac{q_{max} K_L C_e}{1 + K_L C_e} \tag{7}$$

$$\frac{1}{qe} = \frac{1}{q_{max} K_L} \frac{1}{C_e} + \frac{1}{q_{max}} \tag{8}$$

The Freundlich isotherm model explains that the adsorption of contaminants occurs on heterogeneous surfaces and hence it gives information about the quantity of adsorbate adsorbed per unit mass of adsorbent, and the concentration of adsorbate at equilibrium (Ce) (Jisha Kuttiani Ali et al., 2023; Mishra et al., 2017). Eq. (9) and Eq (10) represent Freundlich's isotherm model, and its linear form (Jisha Kuttiani Ali et al., 2023). The linear plot is created by plotting $\ln C_e$ against $\ln q_e$ to compute the values of Freundlich's constant K_f (capacity of adsorption) and n which are obtained. The value of 1/n reveals the intensity of the adsorption process and agrees the process is feasible ($0.1 < 1/n < 0.5$) or not ($1/n > 2$).

$$q_e = K_F C_e^{\,1/n} \tag{9}$$

$$\ln q_e = \ln K_F + \frac{1}{n} \ln C_e \tag{10}$$

The Temkin adsorption isotherm model defines that during adsorption, due to the indirect interaction between adsorbate and adsorbent, the heat of adsorption reduces linearly (Shikuku et al., 2018; Barathi et al., 2013; Sh. Shahmohammadi-Kalalagh et al., 2011). Eqs. (11) and (12) define Temkin isotherm and it's the linear plot. Based on Temkin equation Eq. (6), the plot of the q_e versus $\ln C_e$ gives the Temkin equilibrium binding constant (K_T) and Temkin constant (B_T).

$$q_e = \frac{RT}{B_T} \ln K_T + \frac{RT}{B_T} \ln C_e \tag{11}$$

$$q_e = B_T \ln K_T + \ln C_e \tag{12}$$

The Dubinin–Radushkevich (D–R) isotherm defines the adsorption surface as mainly heterogeneous Eq. (13) represents the D-R model and Eq. (14) shows the linear form (Jisha Kuttiani Ali et al., 2023; Barathi et al., 2013; Ayawei et al., 2017). The plot of ε^2 (Polanyi potential) versus $\ln q_e$ gives the value of β using slope and intercept. Using the value of β, the binding energy E (KJ/mol) was determined by Eq. (15).

$$q_e = q_{max} e^{(-K\varepsilon^2)} \tag{13}$$

$$\ln q_e = \ln q_{max} - K\varepsilon^2 \tag{14}$$

$$E = \frac{1}{\sqrt{2\beta}} \tag{15}$$

The four isotherm models applied for the adsorption of Ni^{2+}, Zn^{2+}, and phenol on conglomerate, and siltstone are summarized in Figures S8-S10, and isotherm parameters are tabulated in Table S2. It can be seen in Figures S8-S10 (a and e), and Table S2, the best linear fits to experimental data with R^2 value greater than 0.99 were obtained for both adsorbents for Langmuir adsorption isotherm. The best fit of the Langmuir adsorption model disclosed that heavy metal ions and phenol followed the monolayer adsorption. The maximum adsorption capacity obtained from the Langmuir adsorption model of siltstone for Ni^{2+}, Zn^{2+}, and phenol is 1.67 mg/g, 1.23 mg/g, and 0.72 mg/g, respectively which is by experimental adsorption capacity such as 1.58 mg/g for Ni^{2+}, 1.19 mg/g for Zn^{2+}

and 0.58 mg/g for phenol. These findings confirmed that monolayer adsorption has the main role in the adsorption of Ni^{2+}, Zn^{2+}, and phenol onto the surface of siltstone under experimental conditions. While, for the conglomerate, Langmuir adsorption isotherm displayed the highest adsorption capacity for Ni^{2+}, Zn^{2+}, and phenol which is not reliable with experimental adsorption capacity. This shows that contaminant removal occurred by various mechanisms including electrostatic interactions, ion exchange, and hydrogen bonding (Jisha Kuttiani Ali et al., 2023; Mishra et al., 2017; Lyu et al., 2018). As seen in Table S2, the R^2 values of other studied isotherm models were not acceptable which indicated that these models could not explain the adsorption processes of Ni^{2+}, Zn^{2+}, and phenol with both soil samples

3.7. Characterization of soil samples after adsorption

To find the changes in conglomerate, and siltstone after the removal of Ni^{2+}, Zn^{2+}, and phenol, soil samples were analyzed after the adsorption, using different characterization methods such as FTIR, XRD, SEM, and EDX. FTIR spectra of contaminants loaded siltstone and conglomerate were shown in Figure S11. As shown in Figures S11 (a), and (b), the spectra of siltstone and conglomerate after adsorption of Ni^{2+}, Zn^{2+}, and phenol were shown as similar to the ones before adsorption (Figure S1). However, the wavenumber area of 1300–750 cm^{-1}, and 2200–750 cm^{-1} were more affected, especially after adsorption of heavy metal ions in siltstone, and conglomerate respectively. Comparison of IR data of both soil samples before and after adsorption provided evidence that different

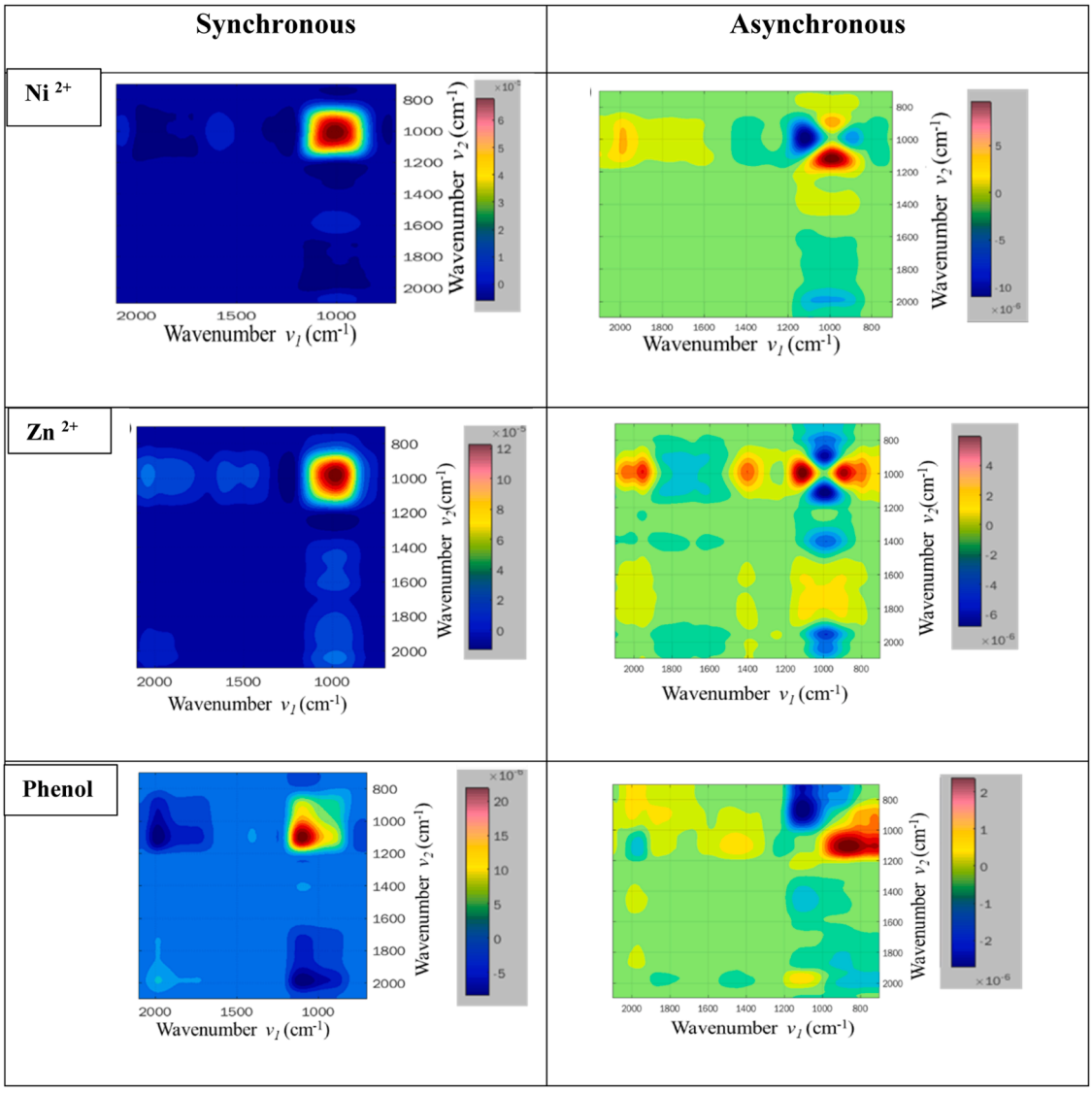

Fig. 6. 2D FTIR synchronous and asynchronous plots of siltstone after Ni^{2+} adsorption, Zn^{2+} adsorption, and phenol adsorption up to 48 h at temperature and without changing the pH.

functional groups such as carboxylate groups, and silicate groups are present in siltstone and conglomerate and they played a significant role in heavy metal chelation during adsorption (Jisha Kuttiani Ali et al., 2023; Lisette D'Souza et al., 2008; Petrella et al., 2019). However, a significant effect on the peaks on both the soil after the phenol adsorption was not noted which indicates less interaction of phenol with soil samples.

In addition, as shown in Figure S12, there is no significant change in the XRD patterns on both the soil samples before and after the adsorption of Ni^{2+}, Zn^{2+} ions, and phenol. This indicated that there were no changes in the crystal planes of both soil samples after adsorption or no incorporation of heavy metals and phenol into the crystal lattice of soil samples. This has further confirmed that the adsorption of heavy metals and phenol was a physisorption-controlled mechanism.

To analyze the changes in the morphology of soil samples after Ni^{2+}, Zn^{2+} ions, and phenol adsorption, SEM analysis was done for both soil samples after Ni^{2+}, Zn^{2+}, and phenol adsorption. As seen in Figure S13, the SEM images of both soil samples after heavy metal ions and phenol adsorption did not display significant changes in their surface compared with Fig. 2(a). The accompanying EDX line spectra and mapping of the conglomerate and siltstone after adsorption of Ni^{2+}, Zn^{2+}, and phenol are summarized in Figures S14-S19. The EDX analysis confirmed the occurrence of Ni^{2+}, and Zn^{2+} ions on the conglomerate, and siltstone surface after the adsorption.

3.8. Removal mechanism studies using 2D-COS FTIR

The removal mechanisms of conglomerate and siltstone primarily rely on physisorption which is essentially the interactions of the adsorbates including Ni^{2+}, Zn^{2+}, and phenol on the adsorbents. This can be investigated in detail by employing 2D-COS FTIR (Jisha Kuttiani Ali et al., 2023). The dynamic FTIR spectra used as the input for 2D-COS FTIR analysis are the spectra of solid samples before and after adsorption at various time intervals, up to 336 h for siltstone and conglomerate. The responses of characteristic modes and their correlations under an external perturbation are displayed by auto-peaks along the diagonal and cross-peaks out-off the diagonal line in asynchronous plot and synchronous plot, respectively, in 2D-COS maps (Jisha Kuttiani Ali et al., 2023; Noda, 2007; Chen et al., 2015). In this study, the 2D-COS FTIR describes the mechanisms depending on the responses and correlations at 2000 cm^{-1}, 1415 cm^{-1}, 1000 cm^{-1}, 1612 cm^{-1}, and 2100 cm^{-1} which correspond to the vibration characteristic bands of CO_3^{2-}, Si-O, carboxylate, and heavy metal carbonyl compounds in FTIR characterization of the soils.

The details of 2D-COS FTIR maps for siltstone adsorption are shown in Fig. 6. In Ni^{2+} adsorption, the appearances of predominant auto-peak at Φ(1000, 1000) and Φ(795, 1000) in the synchronous correlation map represent the presence of Si-O silica at 1000 cm^{-1} and 795 cm^{-1}. The less intense cross-peaks at Φ(1140, 1000), Φ(1612, 1000), Φ(2000, 1000), and Φ(2100, 1000) represent the C-O stretching at 1140 cm^{-1}, C═O carboxylate at 1612 cm^{-1}, CO_3^{2-} at 2000 cm^{-1}, and C═O in heavy metal carbonyl compounds at 2100 cm^{-1} in Ni^{2+} adsorption process (Jisha Kuttiani Ali et al., 2023; Noda, 2007). It is evident that the electrostatic interaction of Si-O and Ni^{2+} ions primarily drives the mechanism due to the major presence of silica in siltstone (43%) with a minor contribution of the other components found in XRF results and FTIR results. On the other hand, the absence of the counterparts of Φ(1612, 1000) and Φ (2100, 1000) in the asynchronous correlation map could be attributed to the in-phase responses of carbonyl groups and silica in siltstone for Ni^{2+} adsorption (Jisha Kuttiani Ali et al., 2023). The in-phase responses of the band at 1000 cm^{-1}, and 795 cm^{-1} to Ni^{2+} adsorption confirm the vibrations from silica in siltstone. Furthermore, the correlations of negative cross-peaks at Φ(1140, 1000) and Φ(2000, 1000) and their corresponding peaks of negative Ψ(1140, 1000) and positive Ψ(2000, 1000) indicate the order of responses of the C-O stretching, Si-O, and CO_3^{2-} to that of Ni^{2+} during the adsorption process

Similarly, the Si-O asymmetric stretching peak at 1000 cm^{-1} also indicates the most predominant interaction with Zn^{2+} in combination with some minor interactions from other bands at 1140 cm^{-1}, 1400 cm^{-1}, 1612 cm^{-1}, and 2100 cm^{-1}. This results in the strongest auto-peak at Φ(1000, 1000) and less intense cross-peaks at Φ(1140, 1000), Φ(1400, 1000), Φ(1612, 1000), Φ(2100, 1000) in the synchronous correlation map of Zn^{2+} absorption. However, the attribution of C═O of heavy metal carbonyl compounds at 2100 cm^{-1} in Zn^{2+} adsorption tends to be a stronger argument than the one observed in Ni^{2+} adsorption due to the appearance of the auto-peak at Φ(2100, 2100); this is not visible in the synchronous map of Ni^{2+} adsorption, and the higher intensity of the cross-peak at Φ(2100, 1000). Similar to the observation in Ni^{2+} adsorption mechanisms, the in-phase of C═O carboxylate and Si-O silica is also detected in the Zn^{2+} adsorption process due to the lack of cross-peak at Ψ(1612, 1000). The positive cross-band at Φ(1400, 1000) going along with its counterpart of positive Ψ(1400, 1000) exhibits a faster response of the peak at 1400 cm^{-1} of symmetric CO_2 carboxylate vibration before the Si-O peak at 1000 cm^{-1}. In addition, the association of the negative cross-band at Φ(1140, 1000) and its positive corresponding band at Ψ(1140, 1000) reveals the out-of-phase responses of the band at 1140 cm^{-1}, and the band at 1000 cm^{-1}, in which the C-O stretching peak at 1140 cm^{-1} gives an earlier response to Zn^{2+} compared to the Si-O peak at 1000 cm^{-1} (Jisha Kuttiani Ali et al., 2023).

Unlike the adsorption mechanisms of Ni^{2+} ions and Zn^{2+} ions, the adsorption mechanism of phenol on siltstone is primarily driven by C-O stretching at 1140 cm^{-1} with a minor contribution of CO_3^{2-} in-plane bending band at 2000 cm^{-1}, which are observed by the auto-peaks at Φ(1140, 1140) and Φ(2000, 2000). The high overlap of the region 1000–1200 cm^{-1} which is a constraint of FTIR analysis, restricts the accurate assignment of whether it is C-O stretching of alcohol functional groups or C-O stretching of carboxylic acid group. However, the positive response of cross-peak at Φ(1408, 1140) points to the same response of the CO_2 carboxylate at 1408 cm^{-1}, and the C-O band. As a result, it is more reasonable to assign the band at 1140 cm^{-1} as C-O stretching in carboxylic acid. Furthermore, the couplings of cross-peaks of positive Φ(1408, 1140) and negative Φ(2000, 1140) and their counterparts of positive Ψ (1408, 1140) and negative Ψ(2000, 1140), respectively, reveal the bonding of C═O carboxylate at 1408 cm^{-1} to O-H group of phenol followed by that of CO_3^{2-} at 2000 cm^{-1} and OH groups of phenol. The latest response goes to C-O carboxylic at 1140 cm^{-1}, and OH groups of phenol. In contrast, the interactions of Si-O bands at 795 cm^{-1}, and 900 cm^{-1} to the phenol of siltstone can be noticed by the cross-peaks at Φ(1140, 795) and Ψ(1140, 900). Hence it is reasonable to assume that the mechanism of phenol adsorption of siltstone is

predominantly driven by the interaction of C-O stretching carboxylic and OH groups of phenol based on hydrogen bonding. The less intense contributions of electrostatic interaction of C═O carboxylate, CO_3^{2-}, and Si-O silica could provide stability to the removal mechanism. The order of response reveals that the electrostatic interaction C═O…O-H and CO_3^{2-}. O-H is more sensitive than the hydrogen interaction.

According to the results from soil characterization, the predominant components of the conglomerate are silica and calcite; the calcite content is higher than that in siltstone. In addition, less intensity of C═O in carboxylate at 1612 cm^{-1}, and C═O heavy metal carbonyl compounds at 2100 cm^{-1} is found in the FTIR spectrum of conglomerate. Therefore, the interactions of the conglomerate and the adsorbates, as shown in Fig. 7, are similar to the observations obtained from 2D-COS FTIR correlation maps of siltstone. In Ni^{2+} adsorption, the mechanism is driven by a Si-O stretching peak at 900 cm^{-1} associated with a lesser contribution of CO_3^{2-} bending at 2000 cm^{-1}. This is revealed by the existence of the auto-peaks at Φ(900, 900) and Φ(2000, 2000). The second auto-peak has a higher intensity than that in the 2D-COS FTIR map of siltstone, which implies a stronger attribution of the CO_3^{2-} band in Ni^{2+} adsorption in conglomerate than that in siltstone. This could be due to a higher content of calcite in the conglomerate. The correlation of positive Φ (2000, 900) and positive Ψ(2000, 900) exhibits the out-of-phase response of the CO_3^{2-} peak at 2000 cm^{-1} before the response of the Si-O peak at 900 cm^{-1}. Possibly, which implies a higher electrostatic interaction of CO_3^{2-} and Ni^{2+} than the electrostatic interaction of Si-O and Ni^{2+} could be the reason. Leaving aside the numerical differences, the interactions of C═O carboxylate at 1400 cm^{-1}, and 1600 cm^{-1} and C-O stretching band at 1140 cm^{-1} to Ni^{2+} in the adsorption of conglomerate are generally similar to those observed in siltstone adsorption.

In Zn^{2+} adsorption, the only auto-peak at Φ(1076, 1076) shows that the most important chemical interaction is in the band at 1076 cm^{-1}. Despite the high overlap in the region, the positive cross-band at Φ(1076, 795) exhibits a similar response as the band at

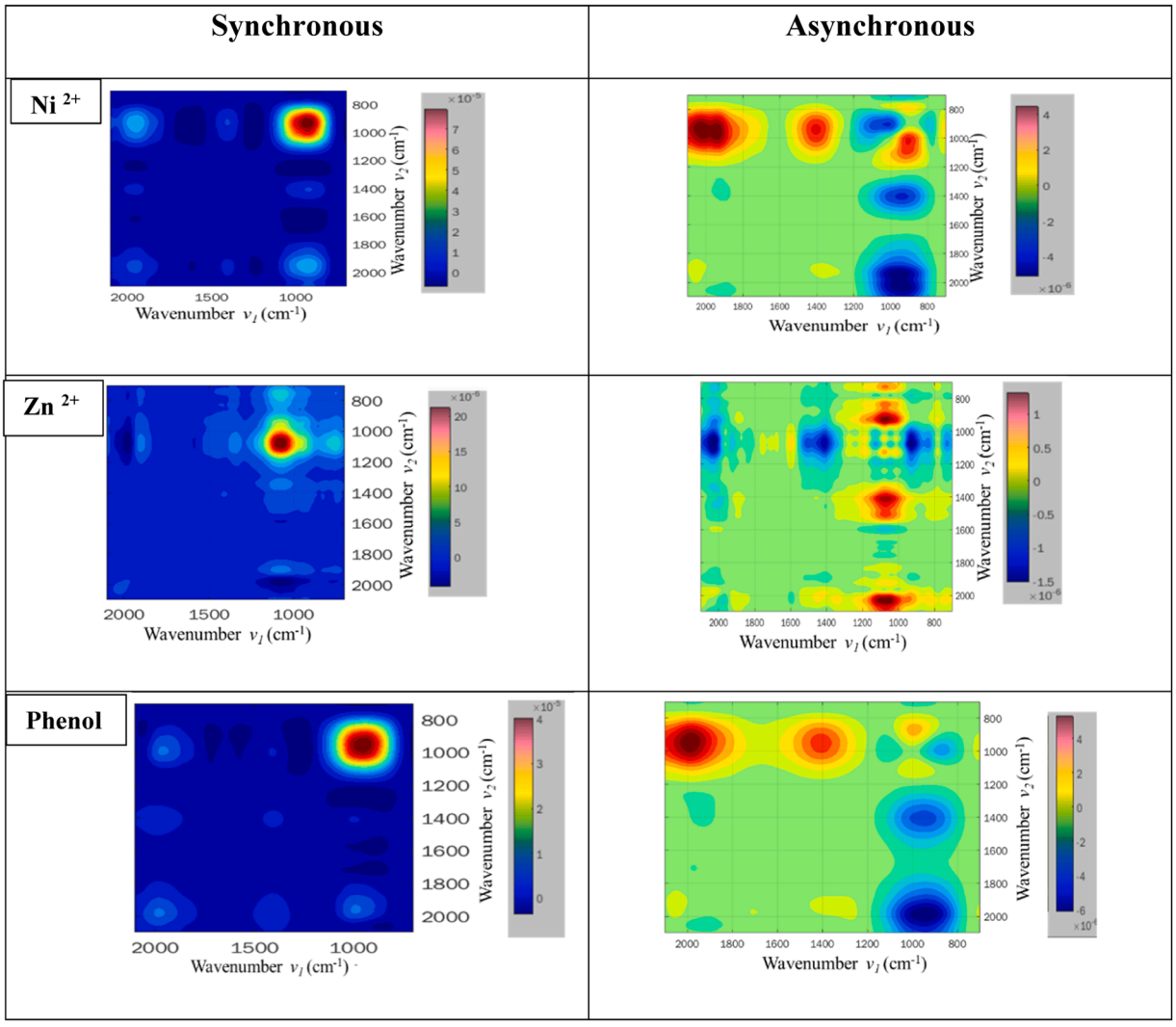

Fig. 7. 2D FTIR synchronous and asynchronous plots of conglomerate after Ni^{2+} adsorption, Zn^{2+} adsorption, and phenol adsorption up to 48 h at temperature and without changing the pH.

1076 cm^{-1}, and the symmetric Si-O stretching at 795 cm^{-1}. Therefore, 1076 cm^{-1} should be reasonably assigned for Si-O asymmetric stretching. In addition, the involvement of C═O heavy metal carbonyl compound at 2100 cm^{-1} in the Zn^{2+} adsorption mechanism of conglomerate is also found to be similar to that in siltstone adsorption. Compared to Ni^{2+}, and Zn^{2+} adsorption, the correlation of strong negative cross-peak at Φ(2100, 1076) in synchronous map and its counterpart of intense negative Ψ(2100, 1076) in asynchronous map implies that the earliest response is due to the C═O peak at 2100 cm^{-1} followed by the Si-O peak at 1076 cm^{-1}. Due to a higher content of calcite in the conglomerate composition, the response of CO_3^{2-} peak at 2000 cm^{-1} in Zn^{2+} adsorption is more possible as shown by the cross-peak at Φ(2000, 1076) compared to that in siltstone adsorption. At the same time, the lower content of carboxyl groups in the conglomerate resulted in the disappearance of responses of bands at 1600 cm^{-1} and 1408 cm^{-1} in synchronous maps. However, the subdued level of Zn^{2+} adsorption mechanisms of conglomerate can still be noticed by the presence of two cross-peaks at Ψ(1400, 1076) and (1600, 1076). Also, although the three peaks at 1076 cm^{-1}, 900 cm^{-1}, and 795 cm^{-1} come from Si-O silica vibration, their responses to Zn^{2+} ions in the adsorption are out-of-phase which is also observed from the Zn^{2+} adsorption mechanism of siltstone. Summing up, the Zn^{2+} adsorption mechanisms of conglomerate and siltstone are primarily similar except for the differences in the intensity of the interferences from the CO_3^{2-} band and C═O carbonyl or carboxylate band depending on the composition of the soil.

Regarding the phenol adsorption mechanisms of conglomerate, the mechanisms are driven by the three bands - Si-O stretching at 920 cm^{-1}, CO_3^{2-} bending at 2000 cm^{-1}, and C═O in carboxylate at 1400 cm^{-1} with a decreasing order in intensity because of the presence of the three auto-peaks of Φ(920, 920), Φ(2000, 2000), and Φ(1400, 1400). The correlations of positive cross-peaks at Φ (2000, 920) and Φ(1400, 920) and their positive counterparts at Ψ(2000, 920) and Ψ(1400, 920) determine the order of the interactions in phenol adsorption (Jisha Kuttiani Ali et al., 2023). The electrostatic interactions of C═O carboxylate at 1400 cm^{-1} and CO_3^{2-} calcite to phenol occur before the interaction of Si-O to phenol at 920 cm^{-1}. Despite the extremely low intensity, the negative cross-peak at (1140, 920) going along with its negative corresponding one at Ψ(1140, 920) shows a possible hydrogen interaction of C-O stretching at 1140 cm^{-1} and phenol. Indeed, the low signal of carboxyl groups in the FTIR characterization of conglomerates not only indicates their lower concentration but also the poor distribution on the conglomerate surface.

We can reasonably say that the adsorption mechanisms of siltstone and conglomerate mainly rely on the interaction of the Si-O band and the adsorbate (Ni^{2+}, Zn^{2+}, and phenol) due to its high content in the soils. However, the contributions of CO_3^{2-} calcite, carboxylate, and carbonyl in heavy metal carbonyl compounds of the soils are significant, especially in the Zn^{2+} adsorption. The order of the responses reveals that the electrostatic interaction of carboxyl groups and CO_3^{2-} groups with the adsorbates is mostly higher than that of Si-O groups. An exception is found in the phenol adsorption on siltstone where hydrogen bonding of C-O from carboxyl groups and O-H from phenol is predominant over the electrostatic interactions; this could be due to the high distribution of C-O bond of carboxyl groups on the siltstone.

4. Conclusion

This research examines the suitability of siltstone and conglomerate obtained from the vadose zone of Abu Dhabi, United Arab Emirates, for the SAT treatment process of PW. The lab scale adsorption investigations revealed that both soil samples exhibited the same removal efficiency for Ni^{2+} (88%) but conglomerate showed a higher removal efficiency for Zn^{2+} (98%) than siltstone. Both soil samples indicate a lower removal performance for phenol, siltstone achieves 32% and conglomerate 9% removal, respectively. The adsorption experimental output was fitted to the Langmuir isotherm for Ni^{2+} and Zn^{2+}, confirming monolayer adsorption. For the removal of Ni^{2+} and Zn^{2+} ions and phenol, soil samples exhibited pseudo-second-order kinetics in equilibrium kinetic experiments. Depending on the correlations in the interactions of functional groups in the soils and the adsorbates found in 2D-COS FTIR, adsorption processes were determined by electrostatic interactions between functional groups (Si-O, CO_3^{2-}, and C═O carbonyl groups) of adsorbent and the Ni^{2+} ions, and Zn^{2+} ions and phenol. Specifically, Zn^{2+} has a greater affinity for carboxyl groups than Ni^{2+}. Except for the preponderance of hydrogen bonding of C-O carboxyl and O-H, we found phenol removal by siltstone owing to the greater stability of the hydrogen bonding in comparison to the electrostatic interactions. Based on the results of this work, siltstone and conglomerate may be employed effectively for SAT treatment, to remove heavy metal ions from oil and gas-generated water. However, it is suggested to eliminate dissolved organic compounds such as phenol, possibly by surface pre-treatment techniques, before applying SAT treatment to PW.

CRediT authorship contribution statement

Hala Ghaleb: Investigation, Data curation. **Jisha Ali:** Writing – review & editing, Writing – original draft, Project administration, Methodology, Investigation, Formal analysis, Data curation, Conceptualization. **Emad Alhseinat:** Writing – review & editing, Supervision, Resources, Project administration, Methodology, Investigation, Funding acquisition, Data curation, Conceptualization. **Kosmas Pavlopoulos:** Writing – review & editing, Supervision, Conceptualization. **Daniel Moraetis:** Writing – review & editing, Supervision, Conceptualization. **Mohamed Soufiane Jouini:** Writing – review & editing, Supervision. **Sasi Stephen:** Writing – review & editing, Investigation. **Tu Phuong Pham Le:** Writing – review & editing, Data curation. **Abdul Fahim Arangadi:** Methodology.

Declaration of Competing Interest

The author(s) declared no potential conflicts of interest with respect to the research, authorship, and/or publication of this paper.

Data availability

Data will be made available on request.

Acknowledgment

This work was financially supported by the Abu Dhabi Award for Research Excellence (AARE-2019) (Award no AARE19–114). The authors are thankful to the Arab Center for Engineering Studies for delivering soil samples. Also, the authors acknowledge Dr. Pakorn Opaprakasit, Center of Excellence in Functional Advanced Materials Engineering Research Center (CoE FAME), Sirindhorn International Institute of Technology for MATLAB code for 2D- FTIR correlation analysis.

Appendix A. Supporting information

Supplementary data associated with this article can be found in the online version at doi:10.1016/j.eti.2024.103604.

References

Al-Jaroudi, S.S., et al., 2007. Use of X-ray powder diffraction for quantitative analysis of carbonate rock reservoir samples. Powder Technol. 175 (3), 115–121.
Ali, A.Ma.E.P., 2014. Quartz surface morphology of Tertiary rocks from North East Sarawak, Malaysia: Implications for paleo-depositional environment and reservoir rock quality predictions. Pet. Explor. Dev. 41 (6), 761.
Ayawei, N., Ebelegi, A.N., and, Wankasi, D., 2017. Modelling and interpretation of adsorption isotherms. J. Chem. 2017, 1–11.
Barathi, M., A.S.K.K, Rajesh, N., 2013. Efficacy of novel Al–Zr impregnated cellulose adsorbent prepared using microwave irradiation for the facile defluoridation of water. J. Environ. Chem. Eng. 1, 1325–1335.
Bruckman, V.J., Wriessnig, K., 2013. Improved soil carbonate determination by FT-IR and X-ray analysis. Environ. Chem. Lett. 11 (1), 65–70.
Caceres-Jensen, L., et al., 2021. Study of Sorption Kinetics and Sorption-Desorption Models to Assess the Transport Mechanisms of 2,4-Dichlorophenoxyacetic Acid on Volcanic Soils. Int J. Environ. Res Public Health 18 (12).
Cai, G.-B., et al., 2010. 1,3-Diamino-2-hydroxypropane-N,N,N′,N′-tetraacetic acid stabilized amorphous calcium carbonate: nucleation, transformation and crystal growth. CrystEngComm 12 (1), 234–241.
Chen, W., et al., 2015. FTIR and synchronous fluorescence heterospectral two-dimensional correlation analyses on the binding characteristics of copper onto dissolved organic matter. Environ. Sci. Technol. 49 (4), 2052–2058.
Flores, C., et al., 2009. Adsorption studies of the herbicide simazine in agricultural soils of the Aconcagua valley, central Chile. Chemosphere 74 (11), 1544–1549.
Gaber, Randa I., Emad Alhseinat, T.P.P.L., Alhseinat, Emad, Nogueira, Ricardo P., Shetty, Dinesh, Hasan, Shadi W., Banat, Fawzi, 2023. *Energy recovery from produced water via reverse Electrodialysis: The role of heavy metals and soluble organics on process performance*. Energy Convers. Manag. 293, 117433.
Grinshpan, M., et al., 2022. On the use of orchards to support soil aquifer treatment systems. Agric. Water Manag. 260.
Guven, O., et al., 2015. Surface morphologies and floatability of sand-blasted quartz particles. Miner. Eng. 70, 1.
Hao, Z., et al., 2018. Cross-scale molecular analysis of chemical heterogeneity in shale rocks. Sci. Rep. 8 (1), 2552.
Hermes, N., et al., 2019. Elucidation of removal processes in sequential biofiltration (SBF) and soil aquifer treatment (SAT) by analysis of a broad range of trace organic chemicals (TOrCs) and their transformation products (TPs). Water Res 163, 114857.
Jisha Kuttiani Ali, H.G., Arangadi, Abdul Fahim, Le, Tu Phuong Pham, Moraetis, Daniel, Pavlopoulos, Kosmas, Alhseinat, Emad, 2023. *Comprehensive assessment of the capacity of sand and sandstone from aquifer vadose zone for the removal of heavy metals and dissolved organics*. Environ. Technol. Innov. 29, 102993.
Ji, J., et al., 2009. Rapid identification of dolomite using a Fourier Transform Infrared Spectrophotometer (FTIR): A fast method for identifying Heinrich events in IODP Site U1308. Mar. Geol. 258 (1-4), 60–68.
Kaczmarek, S.E., et al., 2017. Dolomite, Very High-Magnesium Calcite, and Microbes—Implications for the Microbial Model of Dolomitization. *Charact. Model. Carbonates–Mt. Symp. . 1*.
Kim, Y.Y., et al., 2014. A critical analysis of calcium carbonate mesocrystals. Nat. Commun. 5, 4341.
Kingsley Tamunokuro Amakiri, A.R.C., Marco, Molinari, Athanasios, Angelis-Dimakis, 2022. Review of oilfield produced water treatment technologies. Chemosphere 298, 134064.
Lisette D'Souza, P.D., Divya Shridhar, M.P., Chandrakant, G., Naik, 2008. Use of Fourier Transform Infrared (FTIR) Spectroscopy to Study Cadmium-Induced Changes in Padina Tetrastromatica (Hauck). Anal. Chem. Insights vol. 3, 135–143.
Liu, L., et al., 2021. Biochar aging: Properties, mechanisms, and environmental benefits for adsorption of metolachlor in soil. Environ. Technol. Innov. **24**.
Lyu, H., et al., 2018. Experimental and modeling investigations of ball-milled biochar for the removal of aqueous methylene blue. Chem. Eng. J. 335, 110–119.
Mishra, S.R., et al., 2017. Kinetics and isotherm studies for the adsorption of metal ions onto two soil types. Environ. Technol. Innov. 7, 87–101.
Noda, I., 2007. Two-dimensional correlation analysis useful for spectroscopy, chromatography, and other analytical measurements. Anal. Sci. 23 (2), 139.
Noppadol Sangiumsak, P.P., 2014. Adsorption Behavior of Heavy Metals on Various Soils. Pol. J. Environ. Stud. 23 (3), 853–865.
Petrella, A., et al., 2019. Thermodynamic and kinetic investigation of heavy metals sorption in packed bed columns by recycled lignocellulosic materials from olive oil production. Chem. Eng. Commun. 206 (12), 1715–1730.
Salari, H., et al., 2022. New insights into adsorption equilibrium of organic pollutant on MnO2 nanorods: Experimental and computational studies. J. Mol. Liq. 345.
Sh. Shahmohammadi-Kalalagh, H.B., Nazemi, A.H., Manshouri, M., 2011. Isotherm and Kinetic Studies on Adsorption of Pb, Zn and Cu by Kaolinite. Casp. J. Environ. Sci. 9 (2), 243–255.
Shahata, M.M., 2016. Adsorption of some heavy metal ions by using different immobilized substances on silica gel. Arab. J. Chem. 9 (6), 755–763.
Shahwan, T., et al., 2005. AAS, XRPD, SEM/EDS, and FTIR characterization of Zn2+ retention by calcite, calcite-kaolinite, and calcite-clinoptilolite minerals. J. Colloid Interface Sci. 286 (2), 471.
Sharma, Saroj K., Soil, M.D.K., 2017. aquifer treatment for wastewater treatment and reuse. Int. Biodeterior. Biodegrad. 119, 671.
Shikuku, V.O., et al., 2018. Single and binary adsorption of sulfonamide antibiotics onto iron-modified clay: linear and nonlinear isotherms, kinetics, thermodynamics, and mechanistic studies. Appl. Water Sci. 8 (6).
Sipos, P., et al., 2005. Effect of soil composition on adsorption of lead as reflected by a study on a natural forest soil profile. Geoderma 124 (3-4), 363–374.
Sparks, D., *Environmental Soil Chemistry*. 2nd ed ed, ed. A. Press. 2002, Londo.
Tibbetts, P.J.C., Buchanan, I.T., Gawel, L.J., Large, A., 1992. Comprehensive Determination of Produced Water Composition. , ed. E.S. Research. Vol. 46. In: Ray, J.P., Engelhardt, F.R. (Eds.), Produced Water. Springer, Boston, MA.

Vos, K., Vandenberghe, N., Elsen, J., 2014. Surface textural analysis of quartz grains by scanning electron microscopy (SEM): From sample preparation to environmental interpretation. Earth-Sci. Rev. 128, 93.
Xiao, J., et al., 2022. New strategy for exploring the accumulation of heavy metals in soils derived from different parent materials in the karst region of southwestern China. Geoderma 417.
Yang, Y.J., et al., 2019. Investigating adsorption performance of heavy metals onto humic acid from sludge using Fourier-transform infrared combined with two-dimensional correlation spectroscopy. Environ. Sci. Pollut. Res Int 26 (10), 9842–9850.